PERGAMON

Engineering Fracture Mechanics 68 (2001) 1417–1432

Engineering Fracture Mechanics

www.elsevier.com/locate/engfracmech

Fracture testing and finite element modeling of pure titanium

G.H. Paulino [a], R.D. Carpenter [b], W.W. Liang [c], Z.A. Munir [b], J.C. Gibeling [b,*]

[a] *Department of Civil and Environmental Engineering, University of Illinois, Urbana, IL 61801, USA*
[b] *Department of Chemical Engineering and Materials Science, University of California, One Shields Avenue, Davis, CA 95616, USA*
[c] *Department of Civil and Environmental Engineering, University of California, One Shields Avenue, Davis, CA 95616, USA*

Received 5 March 1999; received in revised form 11 January 2001; accepted 18 January 2001

Abstract

This paper presents the results of fracture experiments and corresponding finite element analyses (FEA) of pure titanium. This investigation was motivated by the desire to develop a *J–R* testing protocol and numerical procedures that are applicable to a titanium/titanium boride layered functionally graded material. Tensile tests and a two-dimensional axisymmetric finite element model were used to determine the plasticity data for the titanium. Crack growth experiments were conducted in three-point bending using single edge notched bend specimens. Three-dimensional FEA of crack growth initiation and two-dimensional FEA with automatic crack propagation were performed. Two crack propagation conditions based on experimental data were used: (a) crack length versus load-line displacement and (b) crack length versus crack mouth opening displacement. The subsequent predictions of the non-linear finite element models are in reasonable agreement with the measured value of *J* at initiation and with the rising *J–R* data during crack propagation.

Keywords: Titanium; Elastoplastic fracture mechanics; Crack resistance curves; *J–R*; Crack mouth opening displacement; Finite element analysis

1. Introduction

In this paper, we present the results of a study that integrates experimental measurements with finite element modeling to describe crack growth initiation toughness and *R*-curve fracture behavior based on *J* in commercially pure titanium (CP Ti). This work was motivated by an interest in combining measurements with modeling to characterize the fracture resistance of a functionally graded material (FGM) based on the titanium/titanium boride (Ti/TiB) system [1]. Functionally graded materials are expected to exhibit significant *R*-curve behavior when one component is a ductile metal [2], although this has not been verified experimentally. For that reason, we wished to incorporate plasticity into a finite element model that describes the interaction of the crack tip stress and strain fields with the material property gradient. Thus, the primary goal of the present study was to develop numerical techniques to model crack tip stresses and strains in a manner that is useful for crack growth initiation and propagation in a FGM. In addition, pure

* Corresponding author. Tel.: +1-530-752-0400/7037; fax: +1-530-752-1031/9554.
E-mail address: jcgibeling@ucdavis.edu (J.C. Gibeling).

0013-7944/01/$ - see front matter
PII: S0013-7944(01)00018-2

titanium was used as a model material to enable the finite element method (FEM) results to be calibrated to experimentally measured parameters.

It was necessary to measure the fracture properties of CP Ti since no relevant experimental data were available in the literature. Titanium exhibits considerable plasticity, hence the J–R response was measured rather than K–R behavior that characterizes more brittle solids [3,4]. In addition, it was necessary to determine the true stress–strain behavior of pure Titanium at strains that are characteristic of the fracture deformation process at the crack tip. These data were incorporated into a FEM model, with the goal of developing predictive capabilities regarding the fracture behavior of Titanium. A number of alternatives exist for simulating crack propagation in finite element analysis (FEA) using discrete [5–7] rather than distributed cracking [8]. For instance, Wawrzynek and Ingraffea [6] have developed a general framework for crack propagation by means of automatic remeshing. Lim et al. [7] have also employed a remeshing technique for crack evolution in an elastoplastic medium. Recently, Trädegård et al. [5] have used the code ABAQUS to model crack propagation in elastoplastic materials by means of a combination of remeshing and nodal relaxation. In this work, we also use the capabilities of ABAQUS to simulate crack growth initiation and stable propagation. The latter is accomplished here by means of a nodal release technique.

The remainder of this paper is organized as follows. First, the experimental procedures are described, including material preparation, the waisted tensile test method to determine the plastic deformation behavior of CP Ti, and the J–R testing. Next the computational approach, using the FEM, is described. In particular, a three-dimensional (3-D) model of crack growth initiation and an automatic two-dimensional (2-D) model of stable crack propagation are presented.

Subsequently, the J–R results of these FEM models are compared with the measured results from fracture tests of the same material. Finally, conclusions are drawn and potential extension of this work is discussed.

2. Experimental methods

2.1. Material preparation

Samples for mechanical testing were machined from a rolled Grade 2 CP Ti plate 13.3 mm in thickness. The nominal composition of this material is 99% titanium. Cylindrical tensile specimens with a gage diameter of 6.35 mm and a gage length of 25.4 mm were turned from bars cut from the plate with the longitudinal axes of the specimens aligned with the rolling direction. Initial tensile tests of these specimens were conducted at a displacement rate of 2.54×10^{-2} mm/s. The resulting fracture surfaces revealed an elliptical cross-section, with major and minor diameters of approximately 5.15 and 4 mm, aligned with the longer axis normal to the thickness direction of the original rolled plate. This observation demonstrated that deformation was significantly anisotropic as a consequence of the strong grain orientation due to rolling. In order to observe the grain structure, samples of material were first ground using silicon carbide paper to 600 grit. They were then polished with 6 and 3 μm diamond on nylon and final polished on a Buehler Vibramet with colloidal silica on flocked cloth. Stain etching with 5% ammonium biflouride was found to be better than Kroll's reagent for revealing the grain structure in optical microscopy. The elongated grains present in the rolled plate are illustrated in Fig. 1(a).

Because an isotropic material was desired to facilitate the fracture studies, heat treatment was employed to eliminate the texture introduced by the manufacturing process. In addition, large grain sizes were desired to gain knowledge of the fracture behavior of large grained titanium for future work on the Ti/TiB FGM system. Isotropic properties were obtained after heating for one hour at 1223 K in a vacuum of 4×10^{-3} Pa followed by cooling to room temperature over a 12 h period. As a result of the annealing heat treatment, the nominal grain size of the material increased 13-fold from about 30 to 400 μm as illustrated in Fig. 1(b).

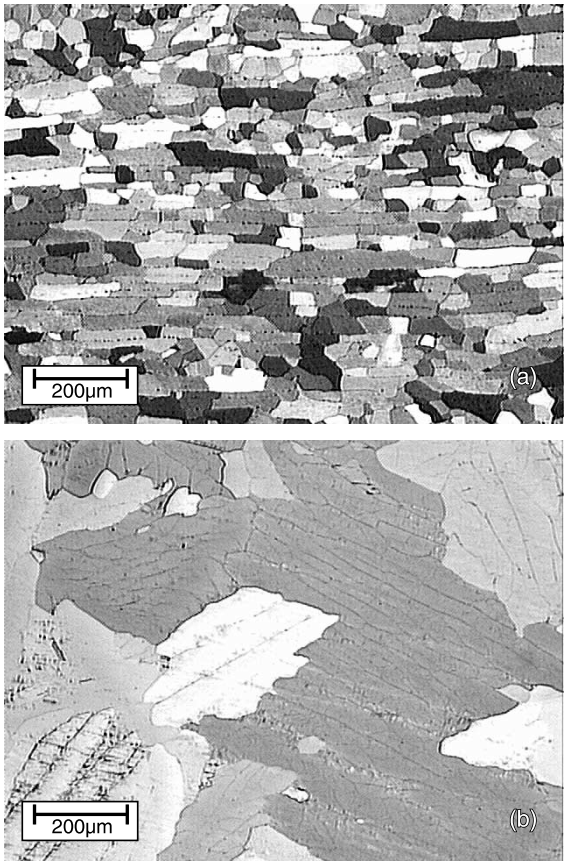

Fig. 1. Optical micrographs of CP Ti in the (a) as-received condition and (b) following heat treatment.

Table 1
Average mechanical properties of grade 2 CP titanium

Material	E (GPa)	Yield strength (MPa)	UTS (MPa)	% Uniform elongation
Grade 2 CP Ti, heat treated (experimental)	106.9	358	500	11
Grade 2 CP Ti [11]	103.4	280	340	–

Correspondingly, the hardness decreased from 87 to 82 on the Rockwell B scale. The fracture surfaces of the annealed specimens exhibited circular cross-sections. The resulting mechanical properties for this CP Ti are summarized in Table 1 along with reference values for Grade 2 titanium obtained from the literature [11].

2.2. Waisted tensile test method

FEM models of crack growth require as input the plastic deformation characteristics at strains beyond the normal limit of uniform tensile deformation under conditions of triaxial loading. In order to determine the true stress–true strain properties of CP Ti, slightly waisted tensile specimens were machined to the dimensions shown in Fig. 2. Three specimens were heat treated as described previously and tensile tested in

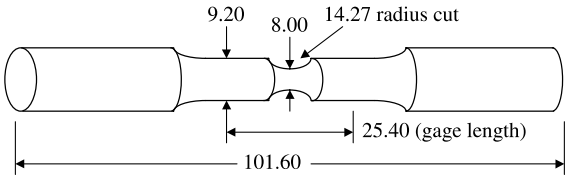

Fig. 2. Waisted tensile specimen used to determine the stress–strain behavior of CP Ti. All dimensions are in millimeters.

uniaxial tension at a rate of 2.54×10^{-2} mm/s using a MTS 632.11B-21 extensometer with a 25.4 mm gage length to measure axial strain and a MTS 632.18E-20 extensometer to measure diametral strain. The waist in the gage section of the specimen permits proper positioning of the diametral extensometer at the neck and monitoring of diametral contraction during the test up to the point of ductile fracture. The axial extensometer was positioned to span the waisted section.

2.3. 2-D axisymmetric waisted tensile FEM model

The true stress–true strain curve for the CP Ti at large strains and constrained flow cannot be measured directly. Rather, these characteristics were determined using a 2-D axisymmetric FEA of the waisted specimen shown in Fig. 2. This model accounts for the symmetry at the mid-length of the specimen. Fig. 3(a) illustrates the corresponding loading and boundary conditions imposed for these calculations. Fig. 3(b) shows the finite element mesh with 363 nodes and 320 four-noded (Q4) elements. The mesh is refined toward the bottom of the model because of high stress and strain concentrations in the area of the waist. The software PATRAN [9] was used for pre- and post-processing, and ABAQUS [10] was used for the analysis.

The material model used in all finite element calculations reported here is for an elastic–plastic power law hardening material obeying the von Mises flow criterion with associated flow rule and isotropic hardening. An iterative procedure was used to obtain the specific parameters to represent the material behavior. The experimental true stress–true strain data from the diametral strain data for one test (Fig. 4(a)) were used as the first input for the material model. The finite element analysis of the waisted tensile specimen was performed to obtain the corresponding engineering stress–nominal axial engineering strain behavior. Here, the nominal axial engineering strain for the model was evaluated directly from the output of the axial extensometer. Similarly, the engineering stress was determined by dividing the load by the initial cross-sectional area in the waisted section. The experimental and FEA engineering stress–nominal axial engineering strain results were then compared (Fig. 4(b)). If the two curves did not match after an iteration, the experimental true stress–true strain curve was shifted vertically until the experimental and corresponding FEA results for engineering stress–nominal axial engineering strain were in agreement. After about 25 iterations, the output shown in Fig. 4 was obtained. The flow behavior determined from this model was used in all subsequent analyses along with a Poisson ratio of $\nu = 0.34$ [12]. Specifically, the results shown in Fig. 4(a) labeled "FEA (final)" were used as the material model for the crack growth analysis by entering the experimental data points individually into the FEA software. We note that this material model describes constrained deformation at strains beyond the normal UTS (in the waist of the tensile specimen). Internally, ABAQUS represents the material behavior using a standard rate-independent J_2 plasticity model accounting for finite strains.

2.4. J–R test method

The titanium plate was cut into single-edge notched bend (SEN(B)) specimens $13.3 \times 25.53 \times 101.6$ mm^3 with a starting notch and integral knife edges in accord with ASTM E399-90 [13] using electro-discharge

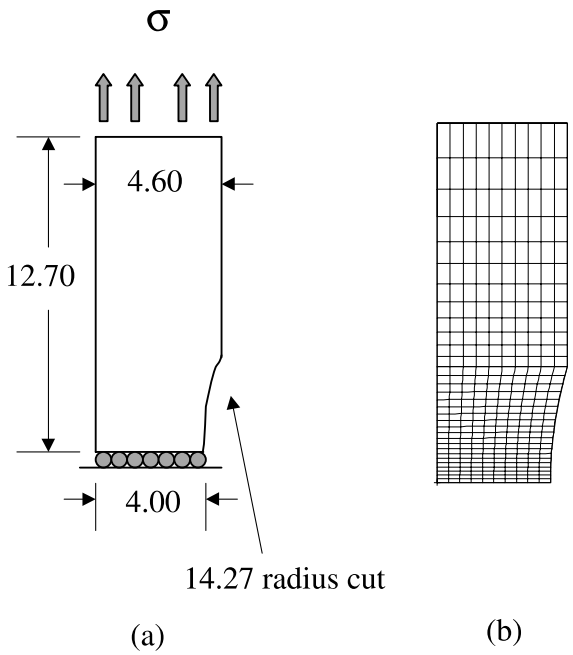

Fig. 3. Tensile test model for Ti (a) loading and boundary conditions imposed in the model, (b) 2-D finite element mesh considering axisymmetry. All dimensions are in millimeters.

machining (EDM). Fig. 5 shows the configuration and orientation with respect to the original plate of the SEN(B) specimens tested in this investigation. The span (88.84 mm) to width (25.53 mm) ratio for this geometry is 3.5, which is less than the recommended ratio of 4.0. Prior to testing, the SEN(B) specimens were heat treated as described previously and cooled overnight to room temperature. Each specimen was pre-cracked in three-point bending using a MTS 810 servo-hydraulic testing machine equipped with a 100 kN model 661.20 force transducer and a MTS 632.03E-30 crack opening displacement gage. Loads were transmitted to the specimen using a bend fixture equipped with 12.7 mm diameter roller supports. The pre-crack was grown in fatigue from an initial machined notch length of 0.4 W to a final crack length of 0.5 W using the MTS 790.40 TestStar II fatigue crack growth test application. The crack was grown at 4 Hz with a load ratio of 0.1 and a final K_{max} of 17 MPa $m^{1/2}$ in accordance with ASTM E1820-96 [14]. The crack length was monitored during pre-cracking by the compliance method based on crack mouth opening displacement.

Four independent J–R tests were conducted in three point bending according to ASTM E1820-96 [14] using the same testing arrangement as for pre-cracking. The specimens were installed in the load frame and cycled 20 times at 2 Hz between 0.45 and 1.98 kN to seat the clip gage. The specimens were then loaded from 0.45 to 4.45 kN at a rate of 0.45 kN/s. In order to determine the initial crack length, the force versus crack mouth opening displacement (CMOD) compliance was then measured three times by reducing the applied load by 1.78 kN and reloading with the testing system operating in load control. Subsequently, the CMOD was increased by 0.0323 mm using CMOD control and the compliance was again measured by the above procedure. After each such increment, the specimens were held for 30 s to allow for crack extension to stabilize, followed by three unloading compliance measurements. The tests were terminated after 30–50 CMOD increments. The crack lengths after testing were then measured by compliance to be about 0.56 W. The specimens were post-test fatigue cracked using a load ratio of 0.5 and a K_{max} of 24 MPa $m^{1/2}$ until the cracks were 0.7 W in length and then broken by application of a monotonic load.

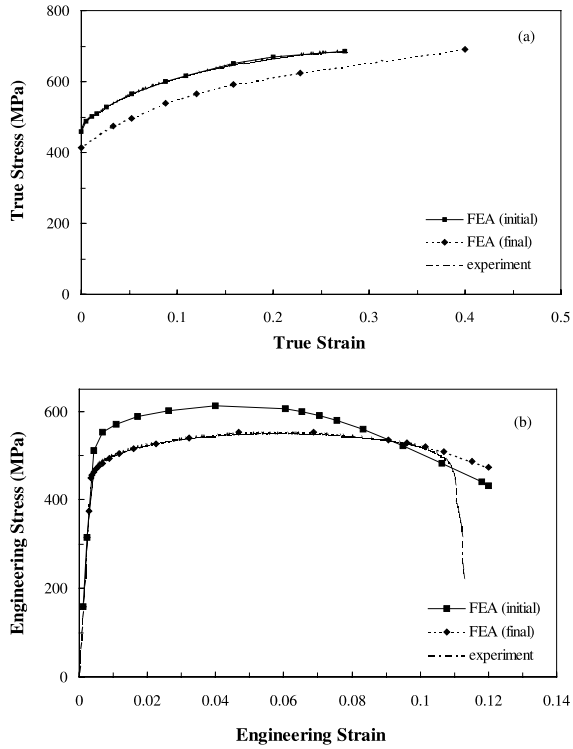

Fig. 4. Results of experiments and iterative finite element analysis to obtain plasticity data for CP Ti (a) true stress based on instantaneous area in the waist versus true strain determined from the diametral extensometer and (b) engineering stress based on initial cross-sectional area in the waist versus nominal axial engineering strain measured by the axial extensometer.

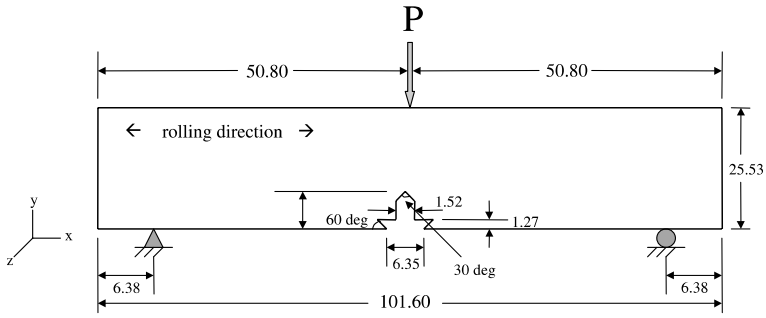

Fig. 5. Single edge-notched specimen for three-point bend testing. The specimen thickness is 13.3 mm. All dimensions are in millimeters.

Crack lengths were computed from the unloading compliance data using the analysis procedures and compliance calibration equations described in the ASTM standard [14]. The three crack lengths determined from the three unloading compliance measurements for each increment of crack extension were averaged. The initial and final crack lengths were measured on the fracture surface in accordance with the standard

using a nine-point average through the thickness and found to be in agreement within 0.005 W with the compliance measured crack lengths. The initial crack front profiles met the straightness criteria of the standard, although the final crack exhibited slightly greater curvature (15% deviation) at the edges than is permissible (5% deviation). In addition, J–R and δ–R curves were determined from the load and load-line displacement data using the procedures described in the standard [14], where δ is the crack tip opening displacement. We note that the load-line displacement data measured using the test machine LVDT were corrected for machine compliance and surface indentation of the specimen at the loading supports. These correction factors were assessed from the load versus load-line displacement behavior of a sandwich specimen composed of CP Ti layers with a stiff steel core tested at loads similar to those encountered in the J–R tests.

3. Computational approach

As noted above, the experiments were conducted in three-point bending using standard SEN(B) specimens. The computational approach involves detailed finite element modeling of the cracked geometry and the calculations have been performed using finite strain assumptions. Thus, it is possible to determine the stress and plastic strain fields in the vicinity of the crack front and their evolution with loading. Initially, crack growth initiation was studied by means of a 3-D FEM model with a stationary crack. Subsequently, a 2-D FEM model for automatic crack propagation was developed. Modeling of the crack tip region for both the 2-D and 3-D configurations is discussed in detail later in this paper. These details can have a significant influence on the finite element analysis results. The software PATRAN [9] was used for pre- and post-processing, and ABAQUS [10] was used for the FEA.

3.1. 3-D model of crack growth initiation

The three-dimensional finite element model of the SEN(B) test specimen (Fig. 5), takes into account two planes of symmetry, one at mid-length and the other at mid-thickness of the beam, as illustrated in Fig. 6. The corresponding finite element mesh is shown in Fig. 7 and contains 9779 nodes and 8200 eight-noded brick (B8) elements. The elements were integrated using reduced integration with hourglass control. Fig. 7(a) and (b) illustrates that the mesh is refined toward the crack front because of high stress and strain gradients in that region. We note that there are 10 layers of elements along the thickness direction (Fig. 7(c)), with discretization refinement as the free surface is approached. From a qualitative point of view, this selective refinement was employed because the free-surface approaches a state of plane stress while the middle surface approaches a state of plane strain. An expanded front view of the crack tip region, which was modeled by blunting the sharp tip, is shown in Fig. 8 (cf. Fig. 7(b)). In an attempt to correlate the mesh with the actual geometry of the pre-cracked beam, the blunting has been performed by means of a quarter circle notch of radius 0.005 mm. Guidelines for selecting an appropriate notch radius can be found in reference [10].

Twentyfive contours for J-integral calculations (see Fig. 8) were investigated during the incremental-iterative FEA such that rings of elements were defined recursively to surround all previous contours. Here, the equivalent domain integral representation was employed to calculate J since this is the most accurate method for FEA [10,15–17]. Theoretically, the J-integral should be independent of the domain. However, J estimates from different rings may vary because of the approximate nature of the finite element solution. Thus, a sufficient number of contours away from and surrounding the crack tip were necessary to obtain a converged value of J in each increment. In the present study, the J calculations were found to converge by the 20th contour. However, to ensure accurate results, J was always evaluated on the 25th contour, which is sufficiently far from the crack tip.

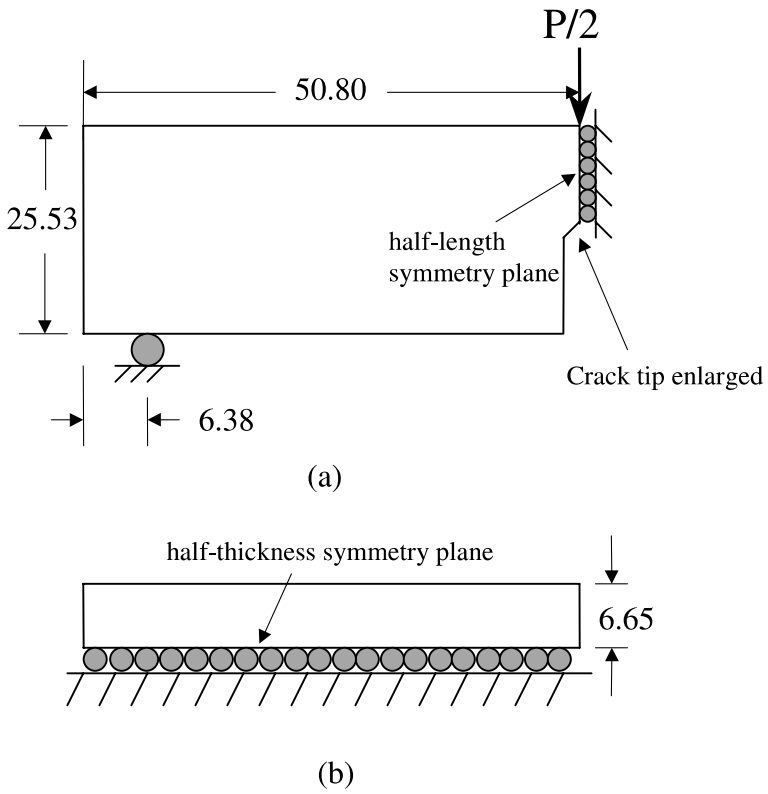

Fig. 6. Loading and boundary conditions imposed in the CP Ti crack growth model: (a) front view, (b) side view.

The FEA was performed under displacement control until the condition for crack growth initiation was reached. Specifically, when the calculated J reached the value of J_Q obtained experimentally, the analysis was stopped, and the numerical values of load, load-line displacement and CMOD were compared with the experimental ones. No additional calibration of this model to the experimental data was performed.

3.2. 2-D model of crack propagation

Although an approximate representation of the J–R behavior of CP Ti could be obtained from the static 3-D model by solving for progressively greater crack lengths, a more thorough treatment must be based on an FEA involving crack propagation. We consider again the edge crack in a CP Ti three-point bend specimen, as illustrated by Fig. 5. In order to describe the stresses, strains and displacements associated with a propagating crack, the notch region was modeled according to the actual geometry of the specimen (compare Figs. 5 and 9) rather than blunting the sharp tip as in the previous 3-D model (Fig. 8). Further, plane strain and finite deformation theory were used in the automatic crack propagation analyses.

Due to symmetry, only one-half of the specimen was analyzed. The mesh is composed of 3872 four-noded quadrilateral (Q4) elements, 4019 nodes, plus 4 reference points as illustrated by Fig. 9. The fourth auxiliary reference point (not shown in Fig. 9) is located near the crack tip and used to measure the crack extension. The loading and support points are simulated by analytical rigid surfaces (cf. Fig. 9) in an at-

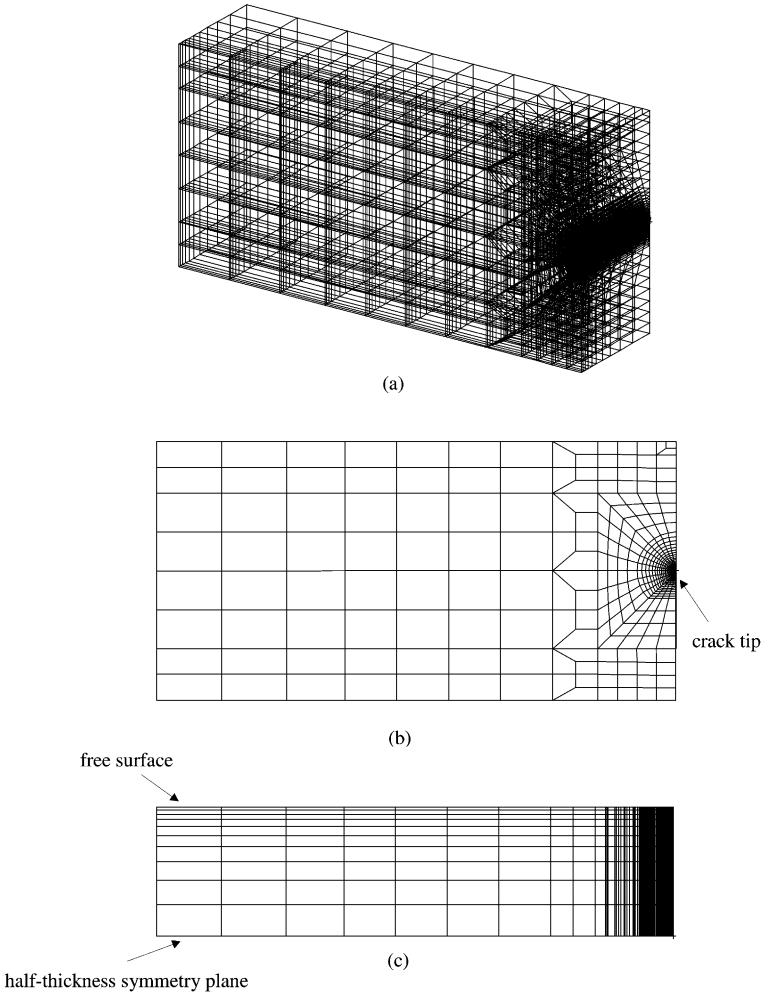

Fig. 7. 3-D FEA model for crack growth initiation considering two planes of symmetry: (a) isometric view, (b) front view and (c) side view.

tempt to resemble the actual conditions in the experiment. The maximum allowable shear stress on the roller support is $\tau_{max} = 100$ MPa. The purpose of imposing a maximum allowable shear stress at the roller supports is to model essentially rigid boundary conditions in a realistic manner. However, the simulations are insensitive to the exact value chosen unless that value is low enough to permit sliding at the interface. A reasonably fine mesh, necessary to obtain an acceptably smooth load versus crack length relation, is used to model the area in which the plastic zone develops and crack propagation occurs. We note that, for the present problem, the crack path is known in advance, and a fine mesh discretization over the entire region where the crack is assumed to propagate is used (Fig. 9).

Initially, a crack length versus load-line displacement condition was used for crack propagation. Because calculations in ABAQUS are carried out in a time-stepped manner, it was necessary to equate load-line displacement with a pseudo-time for purposes of the FEA calculations. For each increment of load-line displacement (or pseudo-time), the solution was allowed to converge. Essentially, this first simulation was

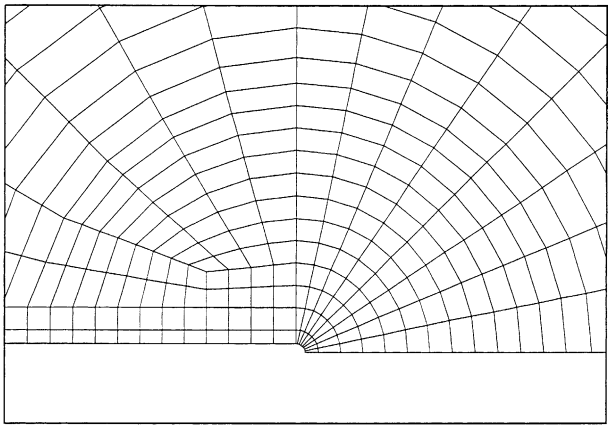

Fig. 8. Expanded view of crack tip region for the 3-D FEA model shown in Fig. 6 illustrating the quarter-circle notch of radius 0.005 mm.

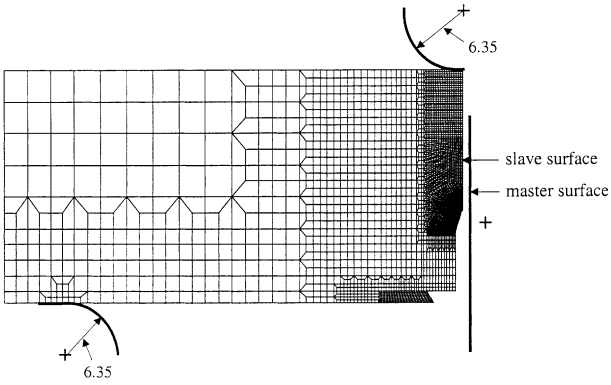

Fig. 9. Basic mesh for 2-D CP Ti crack propagation finite element model. The loading and the support points are simulated by rigid surfaces and three of the four reference points are indicated by the + marks. The fourth reference point is located adjacent to the initial crack tip. All dimensions are in millimeters.

performed to verify the experimental results. Subsequently, a crack length versus CMOD condition was used and compared with the results of the first method. We note that this second analysis used the crack length versus CMOD results obtained from the model based on the crack length versus load-line displacement simulation as input data.

The specimen was subjected to bending loads such that, initially, a well-contained plastic zone developed for the stationary crack. Afterwards, the crack was allowed to propagate. Thus, the FEA was mainly conducted in two phases. The first phase consisted of pushing the rigid surface 1.09 mm downwards, which was the load-line displacement corresponding to the measured J_Q. No crack growth occurred during this stage. In the second phase, the crack was allowed to propagate by means of nodal release along the known crack propagation path. Nodes were released one by one to enable the crack tip to propagate through the mesh. When the fracture condition was met at a node, requiring an increment in crack length for either the current load-line displacement or CMOD, the force at the crack tip node was ramped down according to

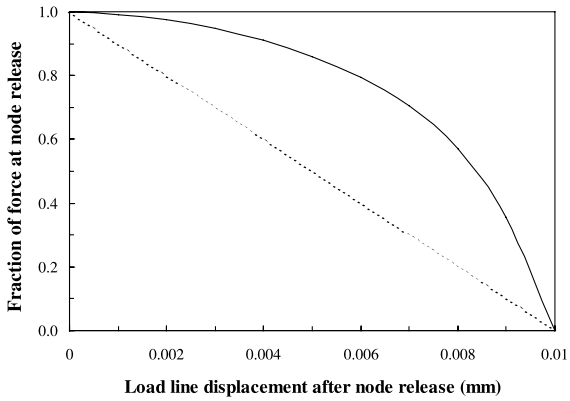

Fig. 10. Force ramp down curve following release at a node in the 2-D crack propagation model.

the solid curve shown in Fig. 10. The manner in which the forces at the released nodes are ramped down can influence the convergence of the solution. In the present study, a fifth order ramp down has been adopted because it leads to a more simulation efficient solution (fewer iterations) than a linear ramp (dashed line).

4. Results and discussion

The experimental results for one J–R test are illustrated in Fig. 11(a) and the corresponding data for crack tip opening displacement (δ–R) are shown on Fig. 11(b). Other tests gave qualitatively similar results. All tests clearly demonstrated the rising J–R response expected for this ductile metal. From these results, preliminary values of J_Q for the annealed pure titanium were calculated from the J–R data and were found to be in the range of 153 to 254 N/mm. We attribute this substantial variability to the coarse grain size of this material (see Fig. 1). Small samples were chosen for this testing due to the limited size of the Ti/TiB

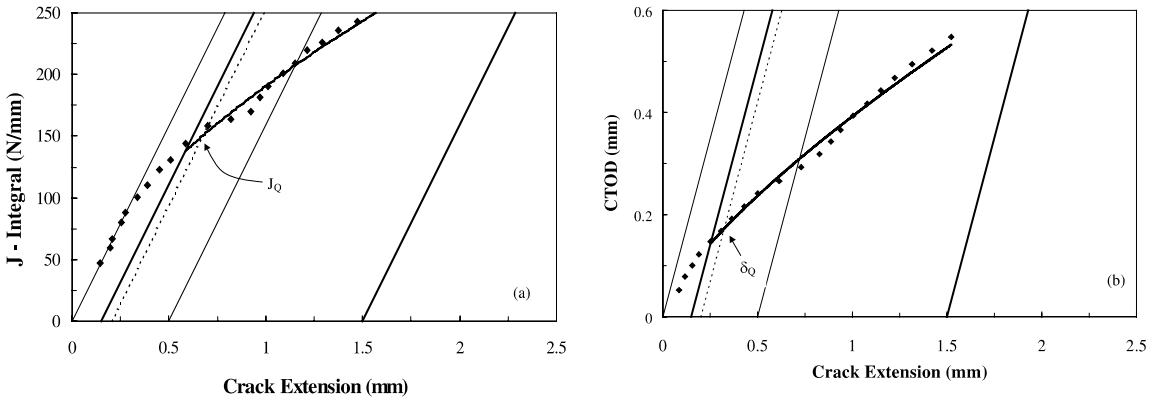

Fig. 11. Results of crack propagation experiments; (a) J–R curve showing measured J_Q value of 153 N/mm and (b) δ–R curve showing measured δ_Q value of 0.170 mm. The construction lines on the plots are defined in ASTM Standard 1820-96 [14].

functionally graded plate [1], which was to be tested using the same fixtures and protocols. The data from this set of experiments on CP Ti were needed to calibrate the elastoplastic finite element model. ASTM E1820-96 requires the specimen size be such that the specimen thickness, $B > 25J_Q/\sigma_Y$ giving a minimum requirement of $B > 28.3$ mm. However, the samples used for these tests were of thickness $B = 13.3$ mm, therefore, this specimen geometry is not of sufficient size to fully meet the ASTM criteria for valid J_{IC} tests of this material. Nevertheless, the experimental results can be directly compared to the results of the computational models, which were constructed for the same specimen dimensions. Due to the rather large scatter in the experimental data, use of an average J value would unnecessarily complicate comparison between model and experiments. Thus, in this study, the data for the specimen with the lowest value of J_Q was used for comparison with the model since this represents the most conservative value.

The results of the 3-D FEA for crack growth initiation are presented in Fig. 12 along with appropriate comparison to experimental results. As noted earlier, the calculations were carried out until $J = J_Q$ corresponding to crack growth initiation. Fig. 12(a)–(c) compares experimental and FEA results for load versus CMOD, J versus load, and load versus load-line displacement, respectively. Fig. 12(d) shows the experimental results for three-point bending and FEA results for both three-point and four-point bending. We note the approximately linear portion of the FEA data, which is essentially the same either for the three-point or four-point configurations. In all cases illustrated in Fig. 12, the experimental and numerical results are in reasonable agreement and show similar trends. However, Fig. 12(d) indicates that the calculated J values are greater than the experimental values at large CMOD. This deviation arises because the model does not account for crack blunting, which contributes to the experimental CMOD. Moreover, the size of the plastic zone at advanced stages of loading also affects the results.

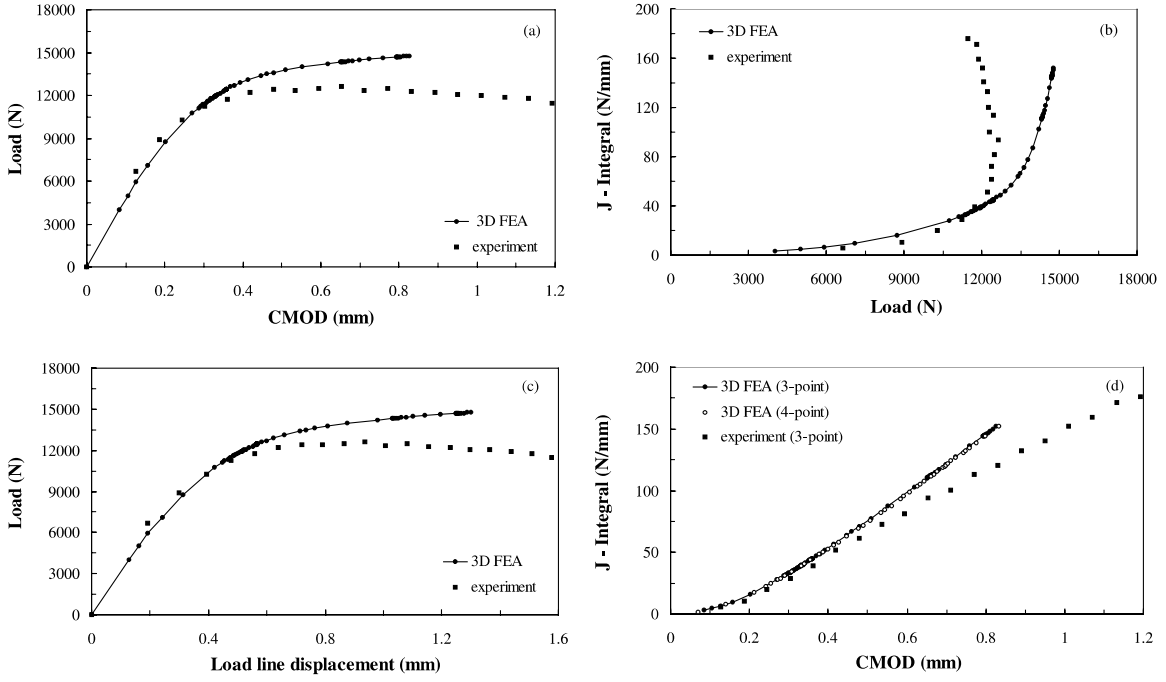

Fig. 12. 3-D FEA results for crack growth initiation: (a) load versus crack mouth opening displacement, (b) J-integral versus load, (c) load versus load-line displacement, (d) J-integral versus crack mouth opening displacement.

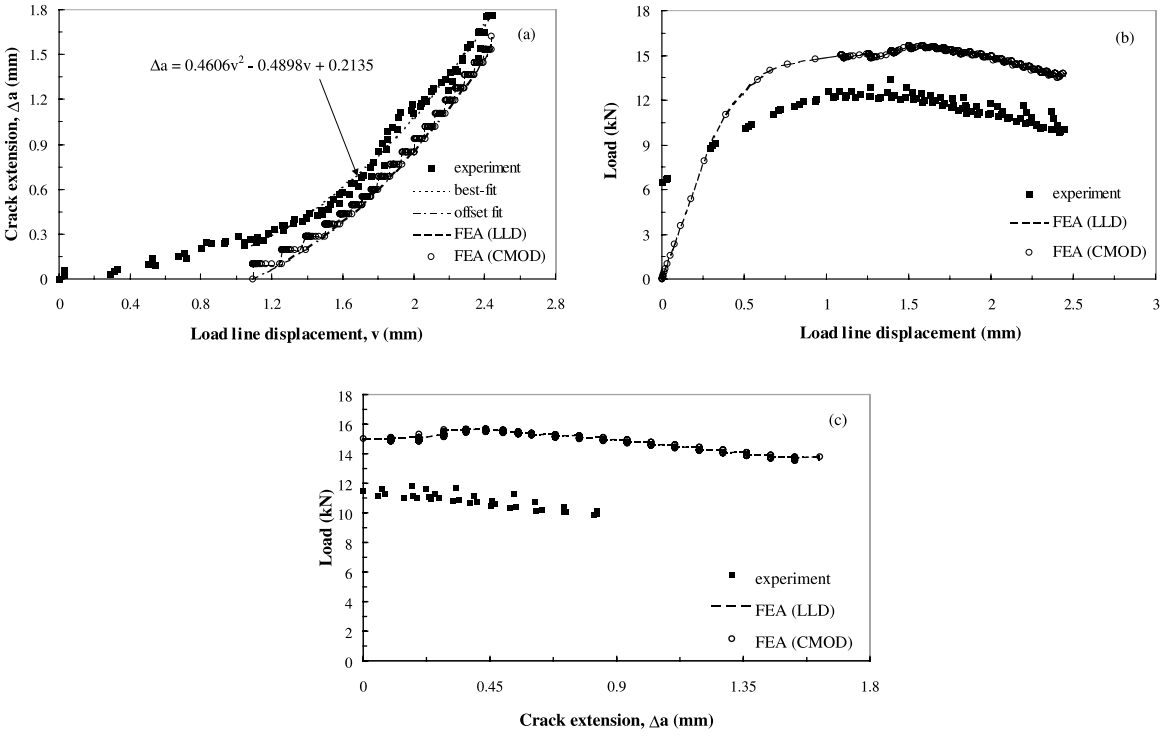

Fig. 13. Results of 2-D FEA of crack propagation based on prescribed crack length versus load-line displacement (FEA LLD) and CMOD (FEA CMOD) simulations illustrating: (a) crack extension versus load-line displacement, (b) load versus load-line displacement, and (c) variation of the reaction force at the rigid loading support as a function of the cumulative crack length (detail).

Results from the 2-D crack propagation FEA model are presented in Fig. 13(a) as accumulated incremental crack extension versus load-line displacement. The increments associated with each nodal release event are apparent in the FEA results. In order to facilitate comparison of the model with the experiments, the measured crack extension versus load-line displacement data were smoothed by fitting the points beyond the blunting region with a second order polynomial as shown in Fig. 13(a) (labeled "best-fit" in the figure). This best-fit quadratic was then shifted vertically to a crack extension value of zero (labeled "offset fit"). This shift was necessary because the present technique for nodal release in the crack propagation model does not permit the initial crack tip blunting deformation to be accurately simulated. Finally, crack growth was modeled by requiring that the FEA analysis match the experimental crack length versus load-line displacement data, and the resulting output is also plotted in Fig. 13(a). In a similar manner, the second analysis was completed by demanding that the FEA analysis match the crack length versus CMOD results. In both cases, the crack extension values are associated with true physical propagation and not blunting. Fig. 13(b) illustrates the variation of the reaction force as a function of the displacement at the rigid body reference node. Fig. 13(a) and (b) illustrate results for both the crack length versus load-line displacement (LLD) and the crack mouth opening displacement conditions. Fig. 13(c) shows the reaction force as a function of the accumulated incremental crack extension. These figures reveal no differences between the FEA results for the crack length versus load-line displacement condition compared to the crack length versus CMOD condition as expected.

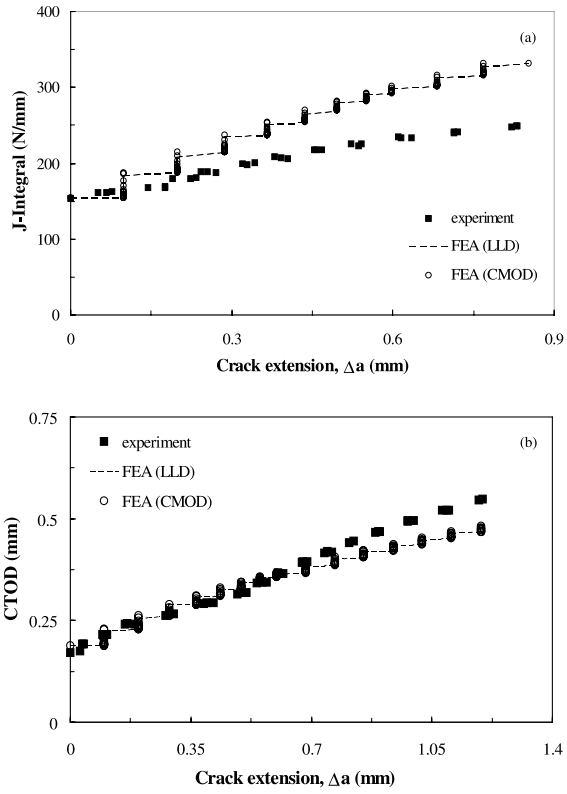

Fig. 14. Resistance curves: (a) J-integral versus post-blunting crack extension; (b) crack tip opening displacement (δ) versus post-blunting crack extension.

The rising portions of the J–R curve for the experimental and computed data are compared in Fig. 14(a). Similarly, Fig. 14(b) shows δ–R curves obtained from experiments and numerical simulations. Again, in both plots, the experimental data have been shifted to exclude the apparent crack extension due to blunting, which is not included in the simulation.

Both experimental and FEA crack tip opening displacements (δ) in Fig. 14(b) have been obtained indirectly. The experimental δ values are based on equations from the ASTM standard [14], while the δ in the FEA was calculated by means of the equation $\delta = d_{\mathrm{n}} J/\sigma_{\mathrm{yield}}$, where σ_{yield} is given in Table 1. The constant $d_{\mathrm{n}} \approx 0.44$ was obtained by matching the experimental crack growth initiation point (post-blunting). Previously, this equation has been applied by Shih [18] to small scale yielding problems, who also showed that d_{n} was in the range 0.4–0.8 for structural steels. Related considerations of finite deformation have been discussed by McMeeking and Parks [19]. Direct FEA calculations of δ considering finite deformation effects and special singular elements at the crack tip have been presented by Dodds [20]. However, special elements were not used in the present FEA simulations. It is worth noting that the experimental and calculated δ–R curves in Fig. 14(b) can be compared only on a qualitative basis because of inherent differences between the ASTM equations (based on beam theory) and the FEA (continuum based on finite deformation).

Finally, Fig. 15 shows the normal stress contour plot at the last increment of the FEA for the crack length versus load-line displacement condition. This plot illustrates the stress levels in the domain and reflects the way in which the crack tip region is modeled for the crack propagation simulations.

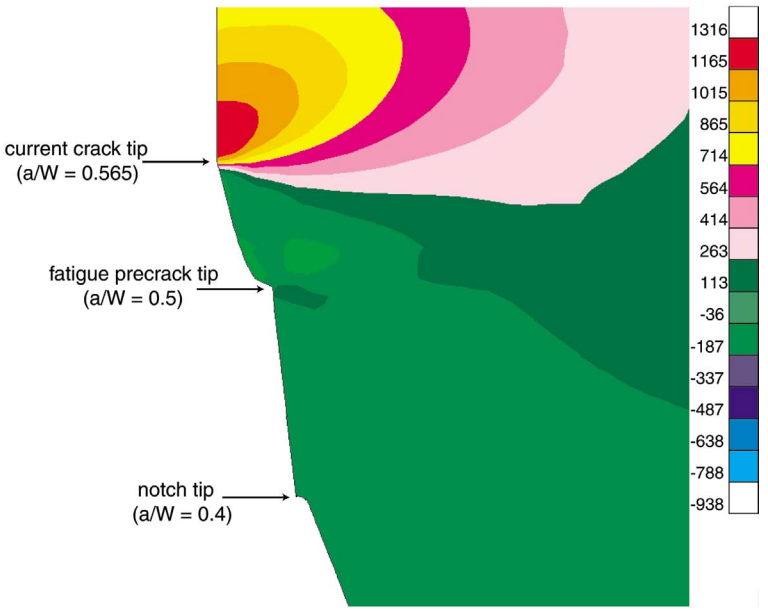

Fig. 15. Normal stress distribution at last increment of 2-D crack propagation model (stresses are in MPa).

5. Conclusions and extension

This study has integrated fracture testing with finite element modeling to describe crack growth initiation and *R*-curve behavior in CP Ti. The experiments were conducted in three-point bending using subsize SEN(B) specimens. A 3-D FEM model was employed for crack growth initiation and a 2-D FEM model was used for automatic crack propagation using a nodal release technique. In general, the predictions of the non-linear finite element model are in good agreement with the corresponding experimental results. In particular, we have developed the methodology to model stable crack propagation with rising *R*-curve behavior in an elastoplastic solid.

This work constitutes a learning experience which will be helpful when dealing with more sophisticated materials such as FGMs. Thus we will extend the *J*–*R* testing protocol and numerical procedures to investigate Ti/TiB layered functionally graded beams under three-point bending. The present results for CP Ti also provide useful information regarding the mechanical properties of one layer of the Ti/TiB FGM beam. This challenging extension is currently under investigation [1].

Acknowledgements

We gratefully acknowledge support of the research described in this paper from the National Science Foundation (NSF) through grant no. CMS-9713798 (Mechanics and Materials Program).

References

[1] Carpenter RD, Liang WW, Paulino GH, Gibeling JC, Munir ZA. Fracture testing and analysis of a layered functionally graded Ti/TiB beam in 3-point bending. Mater Sci Forum 1999;308–311:837–42.
[2] Jin ZH, Batra RC. Some basic fracture mechanics concepts in functionally graded materials. J Mech Phys Solids 1996;44:1221–35.

[3] Atkins AG, Chen Z, Cotterell B. The essential work of fracture and J_R curves for the double cantilever beam specimen: an examination of elastoplastic crack propagation. Proc R Soc London A 1988;454:815–33.
[4] Guinea GV, Pastor JY, Elices M. Stress intensity factor compliance and CMOD for a general three-point-beam. Int J Fracture 1998;89:103–16.
[5] Trädegård A, Nilsson F, Östlund S. FEM-remeshing technique applied to crack growth problems. Comput Methods Appl Mech Eng 1998;160:115–31.
[6] Wawrzynek PA, Ingraffea AR. An edge-based data structure for two-dimensional finite element analysis. Eng Comput 1987;3:13–20.
[7] Lim IL, Johnston W, Choi SK. A finite element code for fracture propagation analysis within elasto-plastic continuum. Eng Fract Mech 1996;53:193–211.
[8] Mosalam KM, Paulino GH. Evolutionary characteristic length method for smeared cracking finite element models. Finite Elements Anal Design 1997;27:99–108.
[9] MSC/PATRAN user's manual, version 7. Los Angeles, CA: The MacNeal-Schwendler Corporation; 1997.
[10] ABAQUS user's and theory manuals, Version 5.7. Pawtucket, RI: Hibbitt, Karlsson and Sorensen, Inc., (HKS); 1998.
[11] ASM metals reference book, 3rd ed. Metals Park, OH: ASM International; 1993. p. 505–11.
[12] Gooch WA, Burkins MS, Palicka R, Rubin J, Ravichandran R. Development and ballistic testing of a functionally gradient ceramic/metal applique. Proceedings of 17th International Symposium on Ballistics, Midrand, South Africa, 1998.
[13] Annual book of standards. Standard E399-90: standard test method for plane strain fracture toughness of metallic materials. Philadelphia, PA: American Society for Testing and Materials; 1997.
[14] Annual book of standards. Standard E1820-96: standard test method for measurement of fracture toughness. Philadelphia, PA: American Society for Testing and Materials; 1997.
[15] Anderson TL. Fracture mechanics fundamentals and applications, 2nd ed. Boca Rotan, FL: CRC Press; 1995. p. 577–85.
[16] Moran B, Shih CF. A general treatment of crack tip contour integrals. Int J Fract 1987;35:295–310.
[17] Shih CF, Moran B, Nakamura T. Energy release rate along a three-dimensional crack front in a thermally stressed body. Int J Fract 1987;30:79–102.
[18] Shih CF. Relationship between the *J*-integral and the crack opening displacement for stationary and extending cracks. J Mech Phys Solids 1981;4:305–26.
[19] McMeeking RM, Parks DM. On criteria for *J*-dominance of crack tip fields in large-scale yielding. ASTM STP 668. American Society for Testing and Materials; 1979. p. 175–94.
[20] Dodds Jr. RH. WARP3D – Static and dynamic nonlinear analysis of solids. Department of Civil and Environmental Engineering, University of Illinois at Urbana, Champaign, 1999.